energies

MDPI

Article

Maximum Perturbation Step Size in MPP-Tracking Control for Ensuring Predicted PV Power Settling Behavior

Teuvo Suntio [1,*] and Alon Kuperman [2]

[1] Electrical Engineering Unit, Tampere University, 33720 Tampere, Finland
[2] Applied Energy Laboratory, Department of Electrical and Computer Engineering, Ben-Gurion University of the Negev, 8410501 Beer-Sheva, Israel; alonk@bgu.ac.il
* Correspondence: teuvo.suntio@tuni.fi; Tel.: +358-400-828-431

Received: 16 September 2019; Accepted: 17 October 2019; Published: 19 October 2019

Abstract: The heuristic perturb-and-observe-based maximum-power-point tracking (MPPT) algorithm of photovoltaic (PV) generator is still the most popular technique in use, despite the broad spectrum of developed other MPPT algorithms. The correct direction of the next perturbation step requires that the previous perturbation is settled down properly and the applied perturbation step size is large enough to overcome the PV-power changes induced by the varying irradiation level and/or the power-grid-originated PV-voltage ripple. The requirements for the minimum perturbation step size are well defined in the available literature. The design equations to predict the PV-power settling time are derived by assuming that the PV-interfacing converter operates in continuous conduction mode (CCM). A large perturbation step size may drive the interfacing converter to enter into discontinuous conduction mode (DCM), which will delay the PV-power settling process and destroy the validity of the predicted settling times. In order to avoid confusing the MPPT process, the maximum perturbation step size has to be limited as well. This paper provides theoretical foundations for the proper design of the maximum step size based on the DC-DC interfacing-converter dynamic behavior. The theoretical findings are validated with experiments as well as by simulations by means of a boost-type DC-DC converter and real PV panel.

Keywords: PV generator; MPP tracking; perturbation step size; transient settling time

1. Introduction

Broad spectrum of maximum-power-point (MPP) tracking algorithms ranging from the simple passive methods to the application of artificial intelligence is available as discussed in [1–6]. The most popular method is still the perturb and observe (P&O) method, where the power of the photovoltaic generator (PVG) is perturbed by applying a step change in the duty ratio or the reference of the input voltage of the PVG-interfacing converter for observing the direction of the PV-power change to selecting the next perturbation step [7–10]. The MPP is reached when the change in the PV power is very small due to the properties of the PV generator (i.e., $dp_{pv}/dv_{pv} \approx 0$) as shown in Figure 1 (cf. p_{pv} at MPP) [11–13]. In reality, the MPP is not just a single point but rather a region, where the PV power change is small (i.e., CPR—constant power region, in Figure 1) [13]. The existence of CPR is also utilized in the MPP-tracking methods known as ripple correlation control or extremum seeking [14].

The MPP can be also found by observing the behaviors of the dynamic ($r_{pv} = -dv_{pv}/di_{pv}$) and static ($R_{pv} = V_{pv}/I_{pv}$) resistances, because r_{pv} equals R_{pv} at MPP as shown explicitly in Figure 2b (i.e., MPP voltage equals 16 V) [11]. This method is known as an incremental conductance (INC) method [15,16].

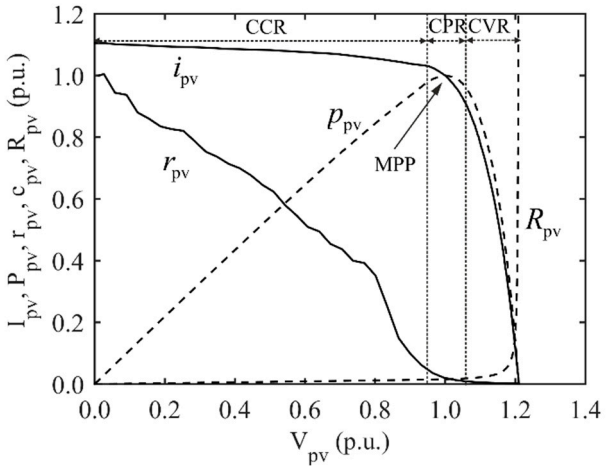

Figure 1. The characteristic per-unit curves of Raloss SR30-36 PV panel (Shanghai Raloss Energy Technology Co. Ltd, Shanghai, PR of China) at the irradiation level of 500 W/m^2, where CCR denotes constant-current region, CVR denotes constant-voltage region, and CPR constant-power region, respectively.

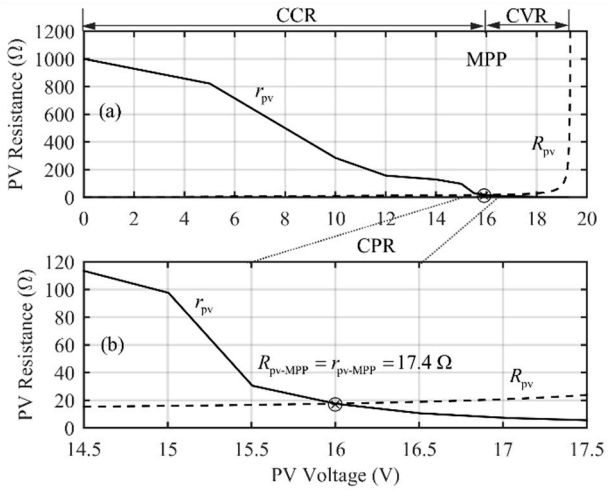

Figure 2. Authentic behavior of the dynamic and static resistances of Figure 1: (**a**) when the PV voltage varies from zero to maximum voltage, (**b**) when the photovoltaic (PV) voltage varies in the vicinity of maximum-power-point (MPP) including CPR.

The P&O and INC methods are, in principle, identical as discussed in [17]. The MPP can be found also by tracking the maximum output current of the interfacing converter as discussed in [18,19]. The output-current-based MPP-tracking processes are not actually studied with similar intensity as the PV-voltage-based MPP-tracking methods, and therefore, the requirements for accurate tracking processes are not explicitly known.

The speed of the MPP-tracking process can be determined by means of the used perturbation frequency and the applied step size [10]. Usually, the perturbation frequency is much less than the switching frequency of the PVG-interfacing converter but Elgendy, et al., [20,21] have proposed and validated MPP-tracking control by using perturbation frequencies equaling the switching frequency of the interfacing converter, which is operated in open-loop mode. The stability of the method and its applicability to the closed-loop-operated interfacing converters are, however, still questionable. The high perturbation step size naturally accelerates the MPP tracking process but leads to the reduction of MPP efficiency as well [10]. The efficiency reduction can be mitigated by adaptively reducing the perturbation step size when approaching the MPP [19,22,23]. The adaptive step-size methods are, however, prone to the drift problem if the minimum step size is incorrectly selected [10].

The perturbation frequency can be adaptive as well, which removes the limitations associated with the adaptive step size as discussed in [24].

As discussed in [25], the most important aspects in MPP tracking is the high tracking accuracy, which guarantees the correct choice of search direction, and the small enough perturbation step size for obtaining high MPP efficiency. The use of the incremental-conductance method is justified for its suitability for tracking the MPP in rapidly changing atmospheric conditions, which are caused by the moving clouds [15]. The dynamic behavior of the moving clouds and their effect on the mismatch losses in PV generators are extensively studied in [26,27]. The outcomes of those studies are summarized in [28], which indicates that the fast MPP tracking would improve the energy outcome only marginally, and therefore, the speed of the MPP-tracking process is not a practical issue as concluded in [25] as well.

It is well defined in the literature that the accuracy of the MPP-tracking process depends on

- the correctly selected perturbation frequency, which guarantees that the PV voltage and current measurements are performed at the moment when the PV power transient is properly settled down [10,12,13,24],
- the correctly selected minimum perturbation step size to producing high enough PV-power variation, which overcomes the combined power changes induced by the irradiation change during the perturbation interval and the PV voltage/current ripple [10,12,13,24].

Nevertheless, it was recently pointed out in [29] that it is also necessary to select correctly the maximum perturbation step size to keep the PVG-interfacing converter to operate and keep on operating in continuous conduction mode (CCM) during the perturbation process. The problem related to the maximum perturbation step size was observed initially when the perturbation dynamics of the boost-type PVG-interfacing converter was modeled and analyzed in [12] and [13]. It was noticed that the accuracy of the analytically predicted settling times was highly dependent on the perturbation step size although the settling-time formulas should be invariant to the perturbation step size [10]. The origin of the problem was traced to the operation mode of the converter, which is assumed to be CCM during the perturbation transients but a too high perturbation step size forced the converter to enter into discontinuous conduction mode (DCM) [29]. This change of mode delayed the settling process and deteriorated the accuracy of the used theoretical formulas to select the correct perturbation frequency as discussed in [29]. The main goal of this paper is to clarify further the problem associated with the maximum perturbation step size.

The rest of the paper is organized as follows: Section 2 introduces briefly the general dynamics of PVG power. Section 3 introduces the theoretical basis for analyzing the step-response input dynamics of the PVG-interfacing converter. Section 4 provides the theoretical formulations for determining the maximum allowed perturbation step size, which keeps the interfacing converter to operating in CCM. Section 5 provides the theoretical and experimental validations of the proposed modeling methods. The conclusions are presented finally in Section 6.

2. General Dynamics of PVG Power

Considering a small perturbation in PVG power, the small-signal PVG power can be given according to [7] as

$$\hat{p}_{\mathrm{pv}} = V_{\mathrm{pv}}\hat{i}_{\mathrm{pv}} + I_{\mathrm{pv}}\hat{v}_{\mathrm{pv}} + \hat{v}_{\mathrm{pv}}\hat{i}_{\mathrm{pv}} \tag{1}$$

based on

$$p_{\mathrm{pv}} = (V_{\mathrm{pv}} + \hat{v}_{\mathrm{pv}})(I_{\mathrm{pv}} + \hat{i}_{\mathrm{pv}}) \tag{2}$$

from which the DC component ($V_{\mathrm{pv}}I_{\mathrm{pv}}$) of the operating point is removed. If considering only the dynamic behavior of the PVG voltage induced by a step change at the operating point of the PV interfacing converter then Equation (1) can be given by

$$\hat{p}_{\mathrm{pv}} \approx V_{\mathrm{pv}}\left(\frac{1}{R_{\mathrm{pv}}} - \frac{1}{r_{\mathrm{pv}}}\right)\hat{v}_{\mathrm{pv}} - \frac{\hat{v}_{\mathrm{pv}}^2}{r_{\mathrm{pv}}} \tag{3}$$

because $\hat{i}_{\mathrm{pv}} \approx -\hat{v}_{\mathrm{pv}}/r_{\mathrm{pv}}$ and $R_{\mathrm{pv}} = V_{\mathrm{pv}}/I_{\mathrm{pv}}$ [12,30]. According to Equation (3) (cf. Figure 2, the behavior of r_{pv} and R_{pv}), we can state that the PVG power ripple can be defined as

$$\hat{p}_{\mathrm{pv}} \approx I_{\mathrm{pv}}\hat{v}_{\mathrm{pv}} \tag{4}$$

in constant current regions (CCR),

$$\hat{p}_{\mathrm{pv}} \approx -\frac{\hat{v}_{\mathrm{pv}}^2}{R_{\mathrm{pv}}} \tag{5}$$

in constant power region (CPR), and

$$\hat{p}_{\mathrm{pv}} \approx -\frac{V_{\mathrm{pv}}}{r_{\mathrm{pv}}} \cdot \hat{v}_{\mathrm{pv}} = V_{\mathrm{pv}}\hat{i}_{\mathrm{pv}} \tag{6}$$

in constant voltage region (CVR), respectively.

Figure 3 shows the behavior of PVG power when the PVG voltage is perturbed by a sinusoidal voltage with 0.5-V amplitude and 50-Hz frequency, and the operating point is swept from the short circuit to open circuit. The behavior of the small-signal PVG power follows exactly the behavior dictated by the equations in (4)–(6) (i.e., constant-amplitude ripple in CCR, very small ripple in CPR, and increasing-amplitude ripple in CVR).

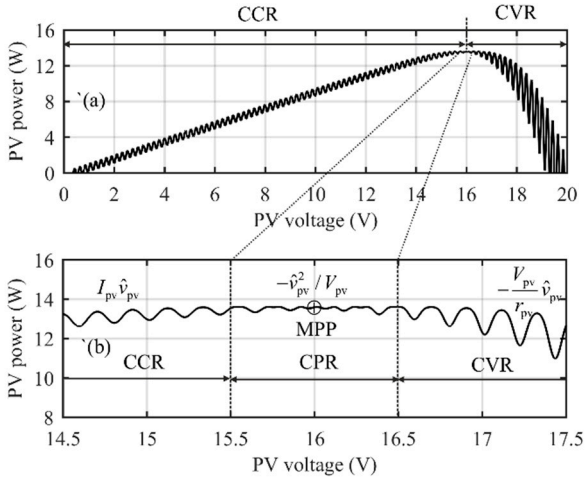

Figure 3. Simulated P-V curve of Raloss SR30-36 PVG (Shanghai Raloss Energy Technology Co. Ltd, Shanghai, PR of China) at the irradiation level of 500 W/m^2, where the PVG-voltage is perturbed with a 100-Hz sinusoidal voltage having the amplitude of 0.5 V: (**a**) the operating points from short-circuit to open-circuit conditions, (**b**) an extended view of the operating points at the vicinity of MPP.

3. General Step-Response Input Dynamics of PVG-Interfacing Converter

The boost-power-stage converter (Figure 4) is a quite popular interfacing converter in two-stage photovoltaic power conversion systems due to its ability to prevent the reverse power flow into the PVG, when the high-side PWM switch is implemented with a diode [31,32]. The use of a diode as a part of the PWM switch also forces the converter to enter into DCM when the inductor current drops to zero. When the high-side switch is replaced by a MOSFET then the operation of converter stays in CCM despite the behavior of the inductor current [32]. The comprehensive dynamic analysis and modeling of the converter can be found from [33–36].

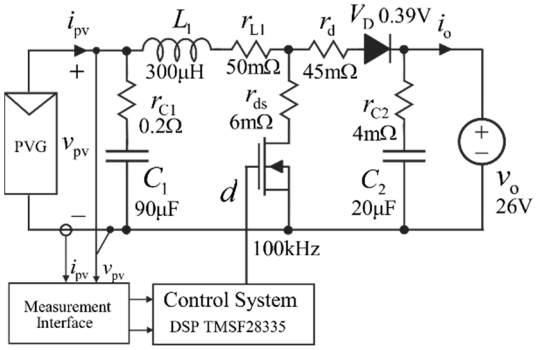

Figure 4. Boost-power-stage converter with the definition of its components, control system, and input/output terminal sources.

The interfacing converter can be used in a photovoltaic application to operate either in an open loop (i.e., the perturbation step change is applied directly to the duty ratio) [13] or in a closed loop (i.e., the perturbation step change is applied to the input-voltage reference) [12].

As shown in Figure 5, the dynamics of the interface between the PVG and its interfacing converter related to the behavior of $\hat{v}_{pv}$ and $\hat{i}_{pv}$ can be given by

$$\begin{aligned} \hat{v}_{pv} &= \frac{Z_{in}}{1+Z_{in}Y_{pv}} \cdot \hat{i}_{ph} + \frac{T_{oi}}{1+Z_{in}Y_{pv}} \cdot \hat{v}_o + \frac{G_{ci}}{1+Z_{in}Y_{pv}} \cdot \hat{c} \\ \hat{i}_{pv} &= \frac{1}{1+Z_{in}Y_{pv}} \cdot \hat{i}_{ph} + \frac{Y_{pv}T_{oi}}{1+Z_{in}Y_{pv}} \cdot \hat{v}_o - \frac{Y_{pv}G_{ci}}{1+Z_{in}Y_{pv}} \cdot \hat{c} \end{aligned} \tag{7}$$

where Z_{in} denotes the input impedance (i.e., $\hat{v}_{pv}/\hat{i}_{pv}$), T_{oi} the reverse transfer function (i.e., $\hat{v}_{pv}/\hat{v}_o$), G_{ci} the control-to-input-voltage transfer function (i.e., $\hat{v}_{pv}/\hat{c}$), and $\hat{c}$ the general control variable (i.e., the duty ratio in open loop, and the input-voltage reference in closed loop) of the PVG-interfacing converter as well as Y_{pv} the output admittance of the PVG.

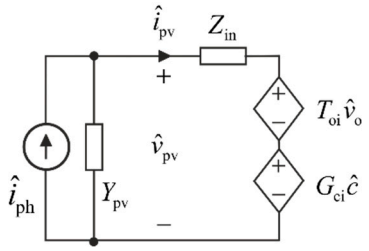

Figure 5. The interface between the PVG and its interfacing converter.

The time-domain behavior of the PVG-power transient can be solved according to (4)–(6) by first solving the time-domain behavior of the PVG voltage by applying inverse Laplace transformation to

$$\hat{v}_{pv}(s) = \frac{G_{ci}(s)}{1 + Z_{in}(s)Y_{pv}(s)} \cdot \frac{\Delta c}{s} \tag{8}$$

where Δc corresponds to the step size applied to the corresponding control input, and $\Delta c/s$ denotes the corresponding step function in the frequency domain. Based on the solved $v_{pv}(t)$, the time-domain behavior of the PVG power, in different operation regions, can be solved based on (4)–(6) as

$$\begin{aligned} p_{\text{pv-CCR}}(t) &= I_{\text{pv-CCR}} v_{\text{pv-CCR}}(t) \\ p_{\text{pv-CPR}}(t) &= -\frac{1}{R_{\text{pv-CPR}}} \cdot v^2_{\text{pv-CPR}}(t) \\ p_{\text{pv-CVR}}(t) &= -\frac{1}{r_{\text{pv-CVR}}} \cdot v_{\text{pv-CVR}}(t) \end{aligned} \tag{9}$$

The behavior of PVG power in different operational regions is solved explicitly in [13] for the open-loop operated and in [12] for the closed-loop operated boost-power-stage converter (cf. Figure 4), respectively. Figure 6 shows the measured dynamic behaviors of the PV power (red), voltage (blue), and current (black) when a step change is applied to the duty ratio of the experimental boost converter in Figure 4. The behavior of the PVG power (red) in Figure 6 indicates that its longest settling time will take place in CCR, and the shortest settling time will take place in CVR when the interfacing converter operates in an open loop.

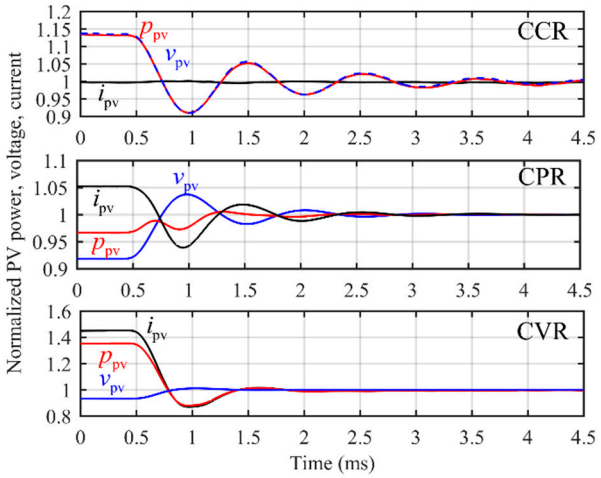

Figure 6. Experimental behavior of PVG voltage (blue), current (black), and power (red) when a step change in the duty ratio of a boost-power-stage converter is applied in different PVG operational regions. All the waveforms are normalized in terms of their final values.

As discussed in [12], the behavior of the closed-loop system (i.e., the complementary sensitivity function) can be estimated by means of the feedback-loop (L) crossover frequency (ω_c) and phase margin (PM). If ω_c and PM do not change but insignificantly when the operating point of the PV generator is varied then the input dynamics of the interfacing converter do not change either. This means that the interfacing converter is invariant to the properties of the PVG, and the PVG-power settling time will be longest in CPR due to its quadratic relation to the PVG voltage as shown in Equation (9) [12]. Therefore, Equation (8) can be given for the closed-loop converter by

$$\hat{v}_{pv}(s) = G_{ci\text{-}c}(s) \cdot \frac{\Delta c}{s} \tag{10}$$

where the closed-loop control-to-input-voltage transfer function ($G_{ci\text{-}c}$) corresponds to the complementary sensitivity function (T) of the closed-loop system (i.e., $T = L/(1+L)$).

The experimental validation of the invariance of the PVG-power settling process to the properties of PV generator, when the PVG interfacing converter is operated under input-voltage feedback control, is performed by using an integral (I) (Figure 7a) and proportional-integral-derivative (PID) (Figure 7b) control methods. The frequency responses of the measured input-voltage feedback loop gains are shown in Figure 7, where ω_c and the corresponding PMs are explicitly given in terms of the operating region of the PVG. The responses show that the PVG affects only marginally the feedback loop gains. According to Figure 7b, the crossover frequency should be placed close to 10 kHz for obtaining perfect invariance to the properties of PVG. The sampling and processing delay of the digital control system (cf. Figure 4) prevents the increasing of ω_c higher than $2\pi \cdot 3$ krad/s in order to maintain a reasonable PM.

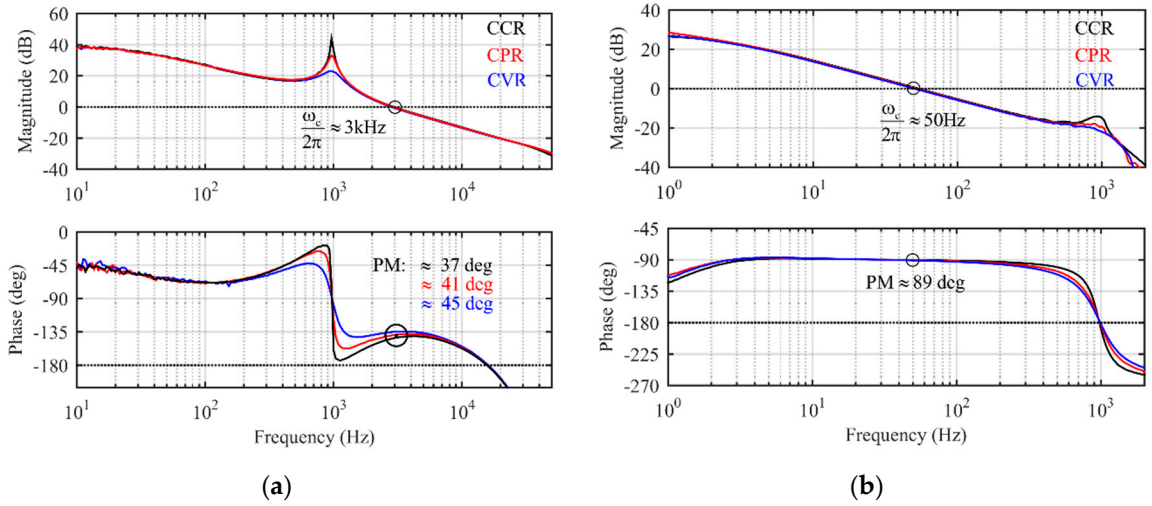

Figure 7. The measured input-voltage feedback-loop gains of the boost-power-stage converter under (**a**) integral (I) control, and (**b**) proportional-integral-derivative (PID) control in the different regions of the PVG.

Figure 8 shows the PVG-power (red), voltage (blue), and current (black) dynamic behaviors when a step in the input-voltage reference of the boost-power-stage converter (cf. Figure 4) is applied in the different operational regions. Figure 8a shows the dynamic behaviors when the I-control method is applied with a rather low crossover frequency and high phase margin (cf. Figure 7a). The figure indicates that the properties of the PVG do not affect the transients. Figure 8b shows the dynamic behaviors when the PID-control method is applied with a reasonable crossover frequency and phase margin (cf. Figure 7b). The figure indicates that the properties of the PVG affect only marginally the transients. When comparing the transient settling times of Figure 8a,b, then it is obvious that the control design determines the duration of the transients.

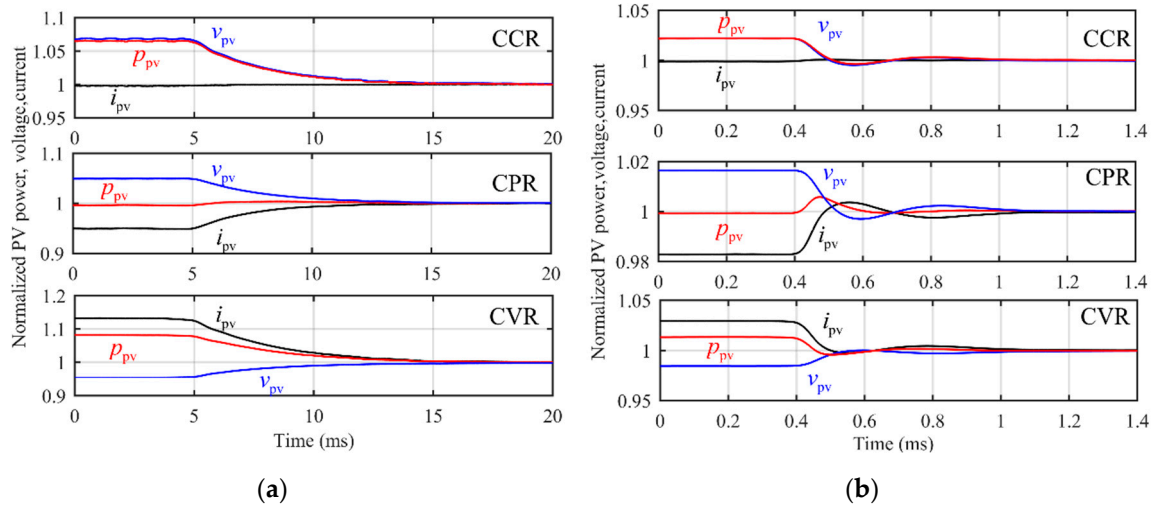

Figure 8. PV power (red), voltage (blue), and current (black) transients under (**a**) I-control and (**b**) PID-control method, when a step is applied to the input-voltage reference of the boost-power-stage converter (cf. Figure 4) in the different operational regions of the PV generator. The transient waveforms are normalized by dividing the waveforms by their final values.

4. Maximum Perturbation Step Size

As discussed in Section 1, the theoretical work in mastering the MPP-tracking control in terms of minimum perturbation step size and maximum perturbation frequency has been already finalized, and

the required theoretical formulations have been fully solved as well [7,10,12,13]. The major residual problem is the maximum allowed perturbation step size in order to keep the PVG interfacing converters to operate in CCM and to ensure the validity of the perturbation-frequency design formulas [29].

In order to derive the theoretical formulations for designing the maximum allowed perturbation step size, the dynamics related to the inductor-current behavior in the interfacing converter have to be determined i.e., the control-to-inductor-current transfer function for the open-loop ($G_{\text{ciL-o}}$) and closed-loop ($G_{\text{ciL-c}}$) operated converters. $G_{\text{ciL-o}}$ can be easily solved from the corresponding state space by solving the transfer functions from the input variables to the state variables (cf. [36] (pp. 383–387) for the boost-power-stage converter). As discussed in [12], the closed-loop control-to-input-voltage transfer function ($G_{\text{ci-c}}$) corresponds to the complementary sensitivity function of the closed-loop converter, which can be estimated based on the crossover frequency and phase margin of the input-voltage feedback loop (cf. Figure 7). The closed-loop control-to-inductor-current transfer function can be derived to be [29]

$$G_{\text{cL-c}} = G_{\text{ci-c}} \cdot \frac{G_{\text{cL-o}}}{G_{\text{ci-o}}} \tag{11}$$

where $G_{\text{cL-o}}$ denotes the open-loop control-to-inductor-current transfer function, and $G_{\text{ci-o}}$ denotes the open-loop control-to-input-voltage transfer function, respectively.

According to above, the time-domain behavior of the averaged inductor current ($\langle i_{\text{L-x}}(t) \rangle$) during the transient can be solved by applying inverse Laplace transform techniques to

$$\begin{aligned} i_{\text{L-o}}(s) &= \frac{G_{\text{cL-o}}(s)}{1 + Z_{\text{in-o}} Y_{\text{pv}}} \cdot \frac{\Delta d}{s} \\ i_{\text{L-c}}(s) &= G_{\text{cL-c}} \cdot \frac{\Delta v_{\text{pv-ref}}}{s} \end{aligned} \tag{12}$$

where Δd and $\Delta v_{\text{pv-ref}}$ denote the corresponding perturbation step sizes and the subscript extensions 'o' and 'c' open and closed loop, respectively. If the systems are of resonant nature then the step response will exhibit overshoot [37]. The overshoot will take place as long as the damping factor (ζ) of the system is less than $1/\sqrt{2}$ [37].

4.1. Open-Loop Operated Boost-Power-Stage Converter

The PVG-affected control-to-input-voltage transfer function ($G^{\text{PV}}_{\text{ci-o}}$) can be given in general according to [13] as

$$G^{\text{PV}}_{\text{ci-o}} = \frac{G_{\text{ci-o}}}{1 + Z_{\text{in-o}} Y_{\text{pv}}} = -V_{\text{e}} \frac{\omega_{\text{n}}^2 (1 + s/\omega_{zC1})}{s^2 + s2\zeta_{\text{pv}}\omega_{\text{n}} + \omega_{\text{n}}^2} \tag{13}$$

where $\omega_{\text{n}} = \sqrt{1/LC_1}$ is the undamped natural frequency, ζ_{pv} is the PVG-affected damping factor (cf. (14)), $\omega_{\text{zC1}} = 1/r_{\text{C1}}C_1$ is the input capacitor induced zero, and $V_{\text{e}} = V_{\text{o}} + V_{\text{D}} + (r_{\text{d}} - r_{\text{ds}})I_{\text{pv}}$ (cf. Figure 4, and [36] (pp. 440–441)).

$$\zeta_{\text{pv}} \approx \frac{1}{2}\left(r_{\text{e}} \sqrt{\frac{C_1}{L}} + \frac{1}{r_{\text{pv}}} \sqrt{\frac{L}{C_1}} \right) \tag{14}$$

where $r_{\text{e}} = r_{\text{L}} + r_{\text{C1}} + Dr_{\text{ds}} + D'r_{\text{d}}$, and the duty ratio can be solved from

$$D = \frac{V_{\text{o}} + V_{\text{D}} - V_{\text{pv}} + (r_{\text{d}} + r_{\text{L}})I_{\text{pv}}}{V_{\text{o}} + V_{\text{D}} + (r_{\text{d}} - r_{\text{ds}})I_{\text{pv}}} \tag{15}$$

The PVG-affected control-to-inductor-current transfer function can be given by

$$G^{\text{PV}}_{\text{cL-o}} = -\frac{sC_1}{1 + s/\omega_{zC_1}} \cdot G^{\text{PV}}_{\text{ci-o}} = \frac{V_{\text{e}} sC_1 \omega_{\text{n}}^2}{s^2 + s2\zeta_{\text{pv}}\omega_{\text{n}} + \omega_{\text{n}}^2} \tag{16}$$

and therefore, (cf. Equation (12)),

$$i_{\text{L-o}}(s) = \frac{V_{\text{e}} C_1 \omega_{\text{n}}^2}{s^2 + s2\zeta_{\text{pv}}\omega_{\text{n}} + \omega_{\text{n}}^2} \Delta d \tag{17}$$

and

$$\langle i_{\text{L-o}}(t) \rangle = V_{\text{e}} C_1 \frac{\omega_{\text{n}}}{\sqrt{1-\zeta_{\text{pv}}^2}} \cdot \exp(-\zeta_{\text{pv}}\omega_{\text{n}} t) \cdot \sin\left(\omega_{\text{n}} \sqrt{1-\zeta_{\text{pv}}^2} \cdot t\right) \Delta d \tag{18}$$

The time t_{min}, when $\langle i_{\text{L-o}}(t) \rangle$ reaches is the minimum value, can be found by setting the first derivate of $\langle i_{\text{L-o}}(t) \rangle$ in (18) to zero, which yields (cf. [37] (p. 160))

$$t_{\text{min}} = \frac{\tan^{-1}\left(\sqrt{1-\zeta_{\text{pv}}^2}/\zeta_{\text{pv}}\right)}{\omega_{\text{n}}\sqrt{1-\zeta_{\text{pv}}^2}} \tag{19}$$

The minimum value of $\langle i_{\text{L-o}}(t_{\text{min}}) \rangle$ can be found based on the envelope behavior of (18) to be

$$\langle i_{\text{L-o}}(t_{\text{min}}) \rangle_{\text{min}} = V_{\text{e}} C_1 \omega_{\text{n}} \exp\left(-\frac{\zeta_{\text{pv}} \tan^{-1}\left(\sqrt{1-\zeta_{\text{pv}}^2}/\zeta_{\text{pv}}\right)}{\sqrt{1-\zeta_{\text{pv}}^2}}\right) \cdot \Delta d \tag{20}$$

The inductor current $i_{\text{L}}(t)$ includes also the ripple component superimposed on the top of $\langle i_{\text{L-o}}(t) \rangle$ and therefore, the requirement for the operation in CCM can be guaranteed when ($I_{\text{pv}} = I_{\text{L}}$ for boost converter)

$$I_{\text{pv}} - \langle i_{\text{L-o}}(t_{\text{min}}) \rangle - \frac{1}{2} i_{\text{L-pp}} \geq 0 \tag{21}$$

The peak-to-peak inductor current of the boost-power-stage converter is highest when the input voltage is half the output voltage, which yields $\Delta i_{\text{L-pp-max}} \approx V_{\text{o}}/(4Lf_{\text{s}})$. Therefore, the maximum duty-ratio step can be given by

$$\Delta d_{\text{max}} < \frac{I_{\text{pv}} - V_{\text{o}}/(8Lf_s)}{V_{\text{e}} C_1 \omega_{\text{n}} \exp\left(-\frac{\zeta_{\text{pv}} \tan^{-1}\left(\sqrt{1-\zeta_{\text{pv}}^2}/\zeta_{\text{pv}}\right)}{\sqrt{1-\zeta_{\text{pv}}^2}}\right)} \tag{22}$$

Equation (22) shows that the converter enters into DCM operation most easily when the irradiation level is low and the duty-ratio step is applied in CCR, where the damping factor ζ_{pv} is smallest and equals $r_{\text{e}}\sqrt{C_1/L}/2$ i.e., the internal damping factor of the interfacing converter (cf. Equation (14), $r_{\text{pv}} >> 1\ \Omega$). The damping of the converter can be increased by applying the similar damping design as in the case of the input-filter design in [38] (i.e., adding in parallel with the input-terminal capacitor a series connection of a capacitor (C_{D}) and a discrete resistor (R_{D}) cf. [38]).

4.2. Closed-Loop Operated Boost-Power-Stage Converter

According to [12] and [37] (pp. 549–552), the closed-loop control-to-input-voltage transfer function ($G_{\text{ci-c}}$) corresponds to the complementary sensitivity function of the closed-loop system, which can be estimated to be of a standard second-order transfer function according to

$$G_{\text{ci-c}} = -\frac{1}{G_{\text{se}}} \cdot \frac{\omega_{\text{n-e}}^2}{s^2 + s2\zeta_{\text{e}}\omega_{\text{n-e}} + \omega_{\text{n-e}}^2} \tag{23}$$

where $\omega_{\text{n-e}}$ denotes the estimated undamped natural frequency, ζ_{e} denotes the estimated damping factor, and G_{se} denotes the sensor gain of the measured feedback variable, respectively. According to [12], ζ_{e}

and $\omega_{\text{n-e}}$ can be given based on the feedback-loop crossover frequency (ω_{c}) and the corresponding phase margin (PM) (cf. Figure 7) as

$$\zeta_{\text{e}} = \frac{\tan(\text{PM})}{2(1+\tan^2(\text{PM}))^{\frac{1}{4}}}\,\omega_{\text{n-e}} = \frac{\tan(\text{PM})}{2\zeta_{\text{e}}}\cdot\omega_{\text{c}} \tag{24}$$

According to Equations (11), (13), and (16), the closed-loop control-to-inductor-current transfer function can be given in general by

$$G_{\text{cL-c}} = -\frac{1}{G_{\text{se}}}\cdot\frac{\omega_{\text{n-e}}^2}{s^2+s2\zeta_{\text{e}}\omega_{\text{n-e}}+\omega_{\text{n-e}}^2}\cdot\left(-\frac{sC_1}{1+s/\omega_{zC_1}}\right) \approx \frac{1}{G_{\text{se}}}\cdot\frac{\omega_{\text{n-e}}^2 sC_1}{s^2+s2\zeta_{\text{e}}\omega_{\text{n-e}}+\omega_{\text{n-e}}^2} \tag{25}$$

when $\omega_{zC_1} = 1/r_{C1}C_1 \gg \omega_{\text{c}}$. If the phase margin of the closed-loop system is rather high (i.e., the poles of the second-order system are well separated) then Equation (25) can be given by

$$G_{\text{cL-c}} \approx \frac{1}{G_{\text{se}}}\cdot\frac{sC_1\cdot\omega_{\text{n-e}}/2\zeta_{\text{e}}}{s+\frac{\omega_{\text{n-e}}}{2\zeta_{\text{e}}}} \tag{26}$$

According to Equation (25), the time-domain behavior of the averaged inductor current $\langle i_{\text{L-c}}(t)\rangle$ during the transient can be given by

$$\langle i_{\text{L-c}}(t)\rangle = \frac{C_1}{G_{\text{se}}}\cdot\frac{\omega_{\text{n-e}}}{\sqrt{1-\zeta_{\text{e}}^2}}\cdot\exp(-\zeta_{\text{e}}\omega_{\text{n-e}}t)\cdot\sin\left(\omega_{\text{n-e}}\sqrt{1-\zeta_{\text{e}}^2}\cdot t\right)\cdot\Delta v_{\text{pv-ref}} \tag{27}$$

Similarly, as in Section 4.1 (i.e., Equations (19) and (20)), the minimum value of (27) is reached when

$$t = t_{\text{min}} = \frac{\tan^{-1}\left(\sqrt{1-\zeta_{\text{e}}^2}/\zeta_{\text{e}}\right)}{\omega_{\text{n-e}}\sqrt{1-\zeta_{\text{e}}^2}} \tag{28}$$

and therefore, the minimum value can be given by

$$\langle i_{\text{L-c}}(t_{\text{min}})\rangle_{\text{min}} = \frac{C_1\omega_{\text{n-e}}}{G_{\text{se}}}\exp\left(-\frac{\zeta_{\text{e}}\tan^{-1}\left(\sqrt{1-\zeta_{\text{e}}^2}/\zeta_{\text{e}}\right)}{\sqrt{1-\zeta_{\text{e}}^2}}\right)\cdot\Delta v_{\text{pv-ref}} \tag{29}$$

The maximum step size of the PVG voltage shall be designed such that $I_{\text{pv}} - \langle i_{\text{L-c}}(t_{\text{min}})\rangle - \frac{1}{2}i_{\text{L-pp}} \geq 0$ ($I_{\text{pv}} = I_{\text{L}}$ for boost converter), which yields (cf. Section 4.1)

$$\Delta v_{\text{pv-ref-max}} < \frac{G_{\text{se}}(I_{\text{pv}} - V_{\text{o}}/(8Lf_s))}{C_1\omega_{\text{n-e}}\exp\left(-\frac{\zeta_{\text{e}}\tan^{-1}\left(\sqrt{1-\zeta_{\text{e}}^2}/\zeta_{\text{e}}\right)}{\sqrt{1-\zeta_{\text{e}}^2}}\right)} \tag{30}$$

According to Equation (30), the interfacing converter will enter into the DCM operation most easily when the irradiation level is low, and the time constant (i.e., $\tau = 1/\zeta_{\text{e}}\omega_{\text{n-e}}$) is small. The maximum step size can be increased by reducing the crossover frequency of the feedback loop and increasing the phase margin.

When the damping factor of the closed-loop system is rather high (cf. Figure 7a) then $\langle i_{\text{L-c}}(t)\rangle$ can be given during the transient according to Equation (26) as

$$\langle i_{\text{L-c}}(t)\rangle = \frac{C_1\omega_{\text{n-e}}}{2G_{\text{se}}\zeta_{\text{e}}}\cdot\exp(-\frac{\omega_{\text{n-e}}}{2\zeta_{\text{e}}}\cdot t)\cdot\Delta v_{\text{pv-ref}} \tag{31}$$

which does not exhibit any kind of overshoot.

5. Experimental and Simulation-Based Validation

The experimental data is produced by using the boost-power-power-stage converter given in Figure 4. The input source is Raloss SR30-36 PVG composed of 36 monocrystalline silicon cells. The PVG was illuminated by fluorescent lamps (cf. Figure 9a), which can produce maximum irradiation of 500 W/m^2 yielding short circuit current of 1.0 A, and open-circuit voltage of 19.2 V at the panel temperature of 45 °C. as well as the MPP at 16 V @ 0.91 A, respectively [39]. The authentic IV-curve of Raloss PVG is given in Figure 9, where the operating points of 10 V (i.e., A), 16 V (B), and 17 V (C) are defined with the corresponding set of V_{pv}, I_{pv}, and r_{pv}, which are used in validating the theoretical predictions.

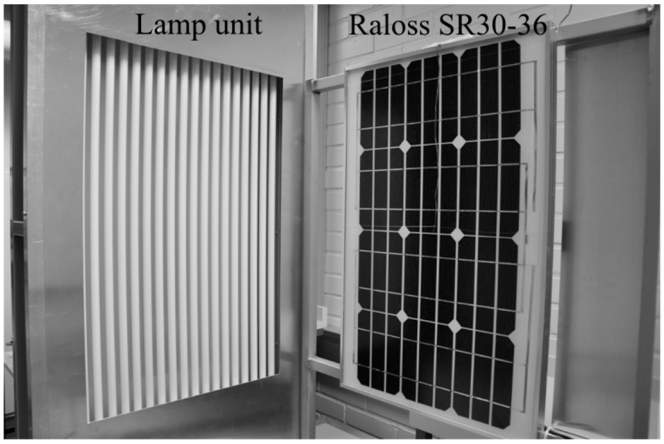

(**a**)

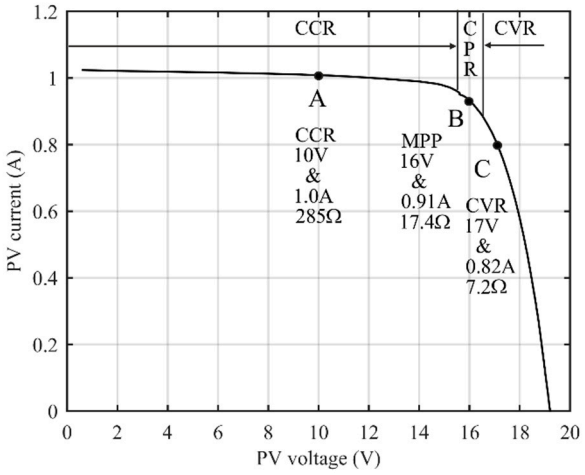

(**b**)

Figure 9. Raloss PVG: (**a**) Its construction and (**b**) authentic PV curve with the operating points A, B, and C.

The interfacing converter was tested in an open loop by applying a step change in its duty ratio in CCR so that the final PVG voltage equaled 10 V (cf. Figure 9, point A). The closed-loop converter was tested under PID-type control (cf. Figure 7b for the feedback-loop specifications) and I-type control (cf. Figure 7a for the feedback-loop specifications) by applying a step change in the PVG-voltage reference in CCR so that the final PVG voltage equaled 10 V (cf. Figure 9, point A). The simulations were performed by constructing a switching model of the interfacing converter and the Raloss PVG in Matlab^{TM} Simulink (R2015a, MathWorks, Natick, MA, USA) environment (cf. [36], (pp. 279–291)), and

applying the same step changes in the corresponding control inputs as in the case of the experimental test. The purpose of the simulations was to verify the behavior of the transients, when the interfacing converter operates in CCM as well as to study the inductor-current behavior, when the maximum step size is applied in different operational regions of the PV generator (cf. Figures 1 and 9 (points A, B, C)).

The type of controller does not play any role in general but the PID controller has to be selected when placing the feedback-loop crossover frequency beyond the resonant frequency, and the I control suffices very well when the feedback-loop crossover frequency is placed at the frequencies lower than the resonant frequency. According to these kinds of control designs, we obtained fast and slowly behaving systems for validating the theoretical predictions.

5.1. Open-Loop Validation

Figure 10 shows the behavior of the PVG voltage (a) and inductor current (b) when the step changes of 0.037 (black), 0.075 (blue), and 0.15 (red) are applied to the duty ratio of the interfacing converter in CCR. According to Figure 4, the damping factor and undamped natural frequency of the boost-power-stage converter can be computed to be 0.074 and 6.1 krad/s, respectively. According to Equation (22), the maximum duty-ratio step will be 0.075, which corresponds to the behavior of the PVG voltage and inductor current with the blue color in Figure 10. The final operating point corresponds to the point A in Figure 9. Figure 10b shows that the predicted maximum perturbation step drives the interfacing converter into the boundary conduction mode (BCM). According to Section 3 (Equation (9)), the PV-power transient in CCR will follow directly the settling behavior of the PV voltage. Figure 10a indicates clearly that the DCM operation delays the settling process when the perturbation step size is larger than the allowed maximum step size.

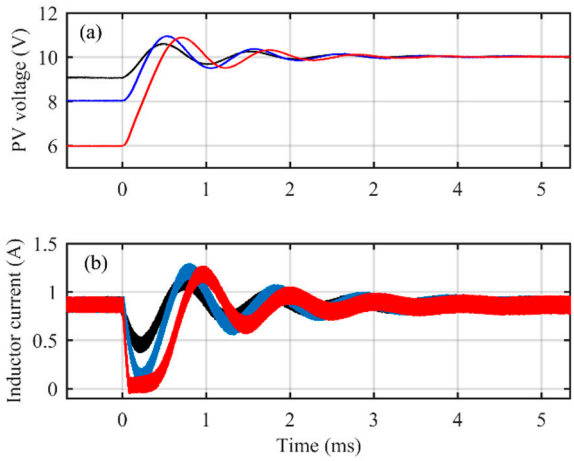

Figure 10. The behavior PVG voltage (**a**) and inductor current (**b**) when step-changes of 0.037 (black), 0.075 (blue), and 0.15 (red) are applied to the duty ratio in CCR.

Figure 11 shows the simulated behavior of the inductor current when the step change of 0.075 in the duty ratio is applied in the open-loop converter in such a manner that the final operating points are 10 V, 16 V, and 17 V (i.e., in different operational regions) (cf. Figure 9, A, B, and C). Figure 11a shows clearly that the CCR behavior of the inductor current stays in BCM. Figure 11b,c show that the inductor current moves towards DCM when the operating point moves to higher voltages, where the initial inductor current is slightly smaller. The change in the damping behavior is also clearly visible, The increase in the damping prevents the inductor current to enter fully into DCM when the PVG current slightly decreases in CPR and CVR compared to CCR (cf. Figure 9, A vs. B and C).

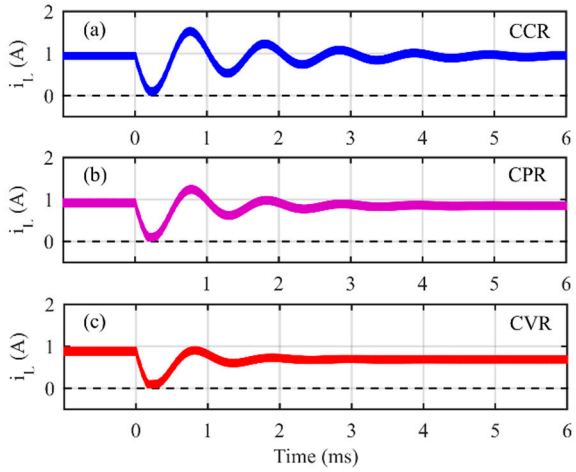

Figure 11. The behavior of inductor current when step-changes of 0.075 is applied (**a**) in CCR, (**b**) in CPR, and (**c**) in CVR.

Figure 12 shows the comparison of the simulated inductor-current behavior (a) and the experimental inductor-current behavior (b) when defined the maximum step size (0.075) is applied in the open-loop-operated boost-power-stage converter. Both of the subfigures show that the inductor current enters into BCM as the presented theory implies. The waveforms are not perfectly identical because of the small differences in the simulation and experimental set ups.

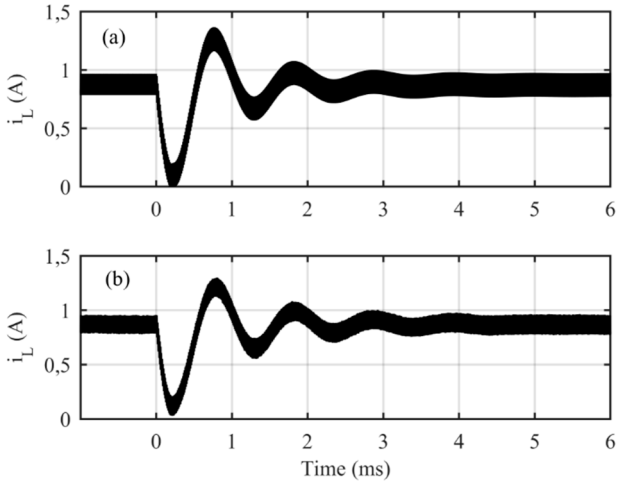

Figure 12. The comparison if the behavior of inductor currents in CCR when the maximum step size (i.e., 0.075) is applied: (**a**) Simulated behavior, and (**b**) experimentally measured behavior.

5.2. Closed-Loop Validation

Figure 13 shows the behavior of the PVG voltage (a) and inductor current (b) when the step changes of 0.5 V (black), 0.71 V (blue), and 3 V (red) are applied to the PVG-voltage reference of the interfacing converter under PID-type control. Based on the measured feedback-loop average crossover frequency (i.e., 18.5 krad/s) and average phase margin (i.e., 35 deg) (cf. Figure 7b), the estimated damping factor and undamped natural frequency (cf. Equation (24)) can be given by 0.32 and 20.5 krad/s, respectively. According to Equation (30), the maximum PVG-voltage-reference step size can be computed to be 0.71 V, respectively. Figure 13b shows that the estimated maximum step size predicts well the boundary operation mode. According to Section 3 (Equation (9)), the PVG-power transient in CCR will follow directly the settling behavior of the PVG voltage. Figure 13a (red curves) shows that the DCM operation delays clearly the settling process when the perturbation step size is

larger than the allowed maximum step size. Figure 14 shows the inductor-current behavior when the maximum step size (0.71 V) is applied in different operational regions. In this case, the inductor current stays close to boundary-conduction mode. Its settling behavior stays quite constant in each region, as Figure 8b (Section 3) implied as well.

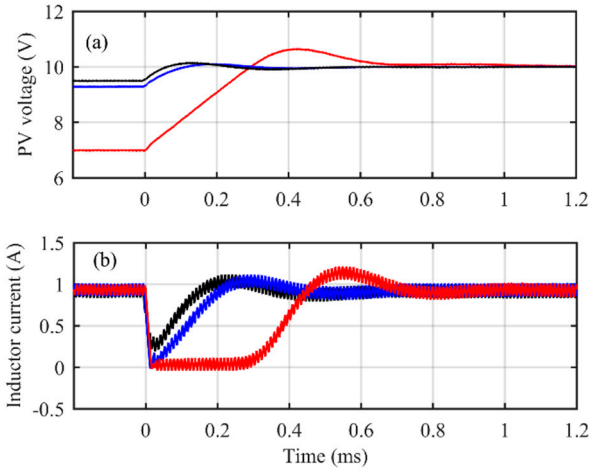

Figure 13. The behavior PVG voltage (**a**) and inductor current (**b**) when step-changes of 0.5 V (black), 0.71 V (blue), and 3 V (red) are applied to the PV-voltage reference of the interfacing converter under PID-type control in CCR.

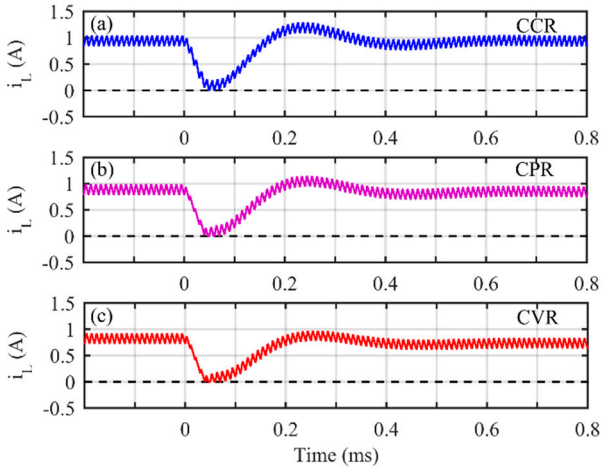

Figure 14. The behavior inductor current when step-changes of 0.71 V is applied (**a**) in CCR, (**b**) in CPR, and (**c**) in CVR.

Figure 15 shows the comparison of the simulated (a) and experimental (b) inductor-current behavior when the predicted maximum step size (0.71 V) is applied. Figure 15 shows that the simulated and experimentally-measured inductor currents reach the boundary conduction mode when the maximum step size is applied as the presented theory implies. The settling behavior of the inductors are not exactly similar due to the uncertainties in the behavior of the controllers (i.e., the simulated control system is based on analog implementation, and the experimental control system is based on digital implementation).

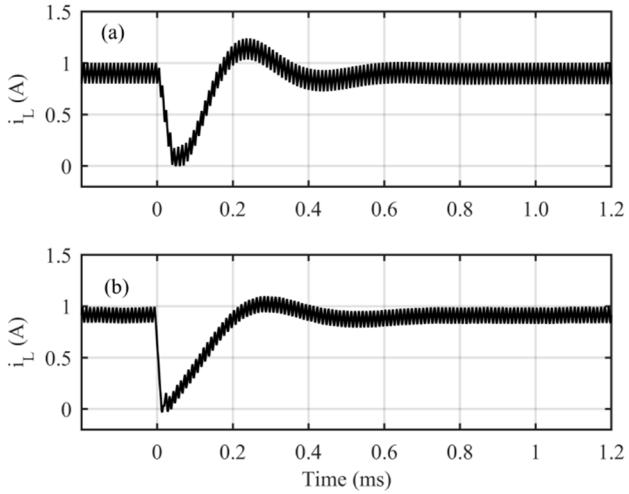

Figure 15. The comparison of the behavior of inductor currents in CCR when the maximum step size (i.e., 0.71) is applied: (**a**) Simulated behavior, and (**b**) experimentally measured behavior.

Figure 16 shows the behavior of the PVG voltage (a) and inductor current (b) when the step changes of 0.9 V (black), 1.8 V (blue), and 2.7 V (red) are applied to the PVG-voltage reference of the interfacing converter under I-type control. Based on the measured feedback-loop crossover frequency (i.e., 314 rad/s) and phase margin (i.e., 89 deg.) (cf. Figure 7a), the estimated damping factor and undamped natural frequency (cf. Equation (24)) can be given by 3.8 and 2.4 krad/s, respectively. The damping factor is so high that the behavior of the PVG voltage would follow the behavior of a first-order exponential function as Figure 16a clearly shows. The applied steps do not cause but insignificant changes in the inductor current as Figure 16b clearly shows. Therefore, there are no limitations to the perturbation step size either.

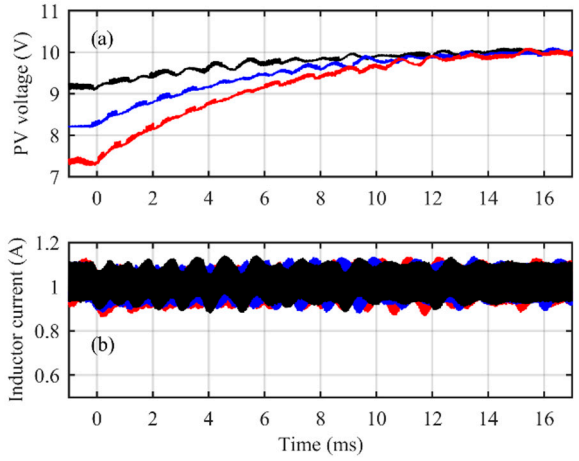

Figure 16. The behavior PVG voltage (**a**) and inductor current (**b**) when the step-changes of 0.9 V (black), 1.8 V (blue), and 2.7 V (red) are applied to the PVG-voltage reference of the interfacing converter under I-type control in CCR.

5.3. Simulation-Based Validation

According to [12], the settling time with resonant-system behavior can be computed according to

$$T_{\Delta}^{\mathrm{PID}} = \frac{1}{\zeta_{\mathrm{e}}\omega_{\mathrm{n\text{-}e}}} \ln\left(\frac{1}{\Delta\sqrt{1-\zeta_{\mathrm{e}}^2}}\right) \tag{32}$$

where Δ denotes the percentage value of the perturbed power step, which is commonly 5% yielding $\Delta = 0.05$, respectively.

Figure 17 shows the simulated PVG-power transients corresponding to the transients in Figure 14. The settling time can be predicted by Equation (32) to be 0.46 ms with $\omega_{\text{n-e}} \approx 20.5$ krad/s and $\zeta_{\text{e}} \approx 0.32$, respectively. Figure 17 shows that the settling time matches with the prediction quite well (i.e., 0.46 ms vs. 0.47 ms, the inaccuracy equals +2.2%). It also shows that the settling time is invariant to the perturbation step size when the interfacing converter operates all the time in CCM. The invariance materializes due to the varying power settling band, which is computed by $\pm\Delta \cdot \Delta P_{\text{pv}}$, where $\Delta = 0.05$ and ΔP_{pv} equals 0.022 W in Figure 17a, 0.033 W in Figure 17b, and 0.138 W in Figure 17c, respectively.

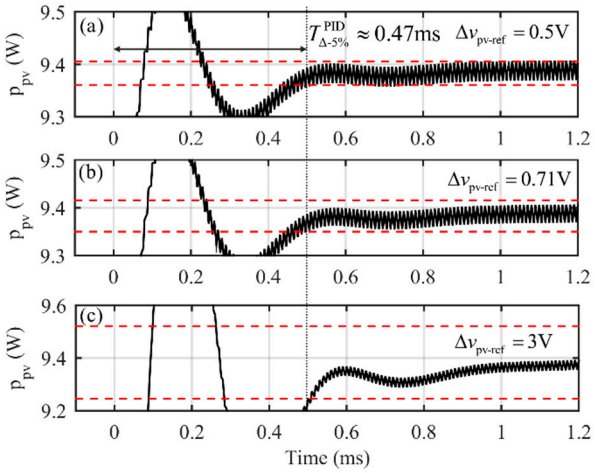

Figure 17. The simulated PVG-power transients when the PVG-voltage-reference step size is (**a**) 0.5 V, (**b**) 0.71 V, and (**c**) 3 V. The converter operates all the time in CCM.

Figure 18 shows the simulated behavior of the inductor current (c), the PVG voltage (b) as well as the PVG power (a) when the perturbation step size equals 3 V (cf. Figure 13, red curves). The red curves correspond to the DCM operation and the blue curves to the CCM operation, respectively. The PV-power settling band is computed as described above (cf. Figure 17). Figure 18a shows that the DCM operation delays the settling process significantly (i.e., the settling time in CCM operation equals 0.47 ms and in DCM operation 0.88 ms, the increase equals 87%).

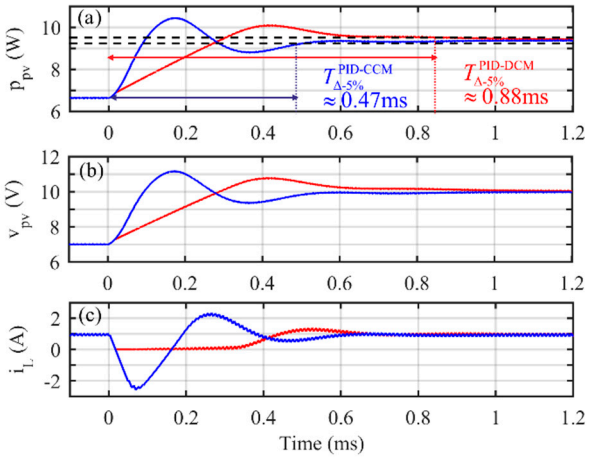

Figure 18. The simulated PVG power (**a**), PVG voltage (**b**), and inductor-current (**c**) transients when the PVG-voltage-reference step size is 3 V. The red curves correspond to the situation, where the interfacing converter enters into DCM. The blue curves correspond to the situation, where the interfacing converter operates all the time in CCM.

5.4. Discussions

According to Equations (22) and (30), the maximum allowed perturbation step size is directly dependent on the level of the inductor current, which depends on the level of irradiation as well. The relation between the PVG current and the inductor current depends on the power stage of the interfacing converter: $I_L = I_{pv}$ for a boost-type converter, and $I_L = I_{pv}/D$ for a buck and buck-boost-type converter (cf. [36] (pp. 376–390)). Due to the direct relation of the inductor current to the level of irradiation, the application of the maximum perturbation step size would require to adjust it adaptively according to the variations in the PVG current.

The maximum allowed step size in the duty ratio for the open-loop-operated boost converter was computed to be 0.075, which corresponds to 2 V in the PVG voltage. The corresponding maximum step size for the closed-loop-operated converter was computed to be 0.71 V, which is much lower than the corresponding step size for the open-loop operated converter. This can be explained by the large differences in the time constants (i.e., $\tau = 1/\omega_n\zeta$) of the converters—2.2 ms (open loop) vs. 0.15 ms (closed loop), which indicates that the open-loop system is more sluggish than the closed-loop system.

6. Conclusions

The P&O-based MPP-tracking control is already well mastered with design formulas, which are developed assuming the interfacing converter to operate in CCM. The paper shows explicitly that the PVG-power settling time is invariant to the perturbation step size when the interfacing converter operates in CCM as the existing design formulas assume.

It has turned out that such an interfacing converter, where the PWM switch contains a diode, can enter into DCM operation due to a too large perturbation step size, and the settling of the PVG power will be delayed compared to the operation in CCM. This phenomenon may lead to a situation where the MPP-tracking process will be confused due to the selection of a wrong direction of the next perturbation step.

This paper has developed the theoretical formulas to determine the maximum allowed perturbation step size for a boost-power-stage converter. The method to develop the formulas is not by no means limited to the named converter but it is generally applicable for the DC-DC converters, which are applied usually in the two-stage grid-connected PV systems.

The developed maximum-perturbation-step-size formulas explicitly show that the maximum step size is directly related to the PVG current, which actually necessitates tuning the maximum step size adaptively, according to the operational conditions in PVG. The formulas show also that the maximum step size is inversely related to the undamped natural frequency of the system, which may vary, especially, in the open-loop-operated converters according to the value of duty ratio and therefore, careful considerations are needed.

Author Contributions: T.S. wrote the paper and performed the simulation-based validations, A.K. performed the proof reading and provided the theoretical background.

Funding: This research received no external funding.

Acknowledgments: Jyri Kivimäki has carried out the original experimental measurements during his PhD studies. The authors appreciate very much that he allowed us to reproduce some of the experimental material.

Conflicts of Interest: The authors declare no conflict of interest.

References

1. Chen, P.-C.; Chen, P.-Y.; Liu, Y.-H.; Chen, J.-H.; Luo, Y.-F. A comparative study on maximum power point tracking techniques for photovoltaic generation systems operating under fast changing environments. *Sol. Energy* **2015**, *119*, 261–276. [CrossRef]
2. Lyden, S.; Hague, M.E. Maximum power point tracking techniques for photovoltaic systems: A comprehensive review and comparative analysis. *Renew. Sustain. Energy Rev.* **2015**, *52*, 1504–1518. [CrossRef]

3. Liu, Y.-H.; Chen, J.-H.; Huang, J.-W. A review of maximum power point tracking techniques for use in partially shaded conditions. *Renew. Sustain. Energy Rev.* **2015**, *41*, 436–453. [CrossRef]
4. Kamarzaman, N.A.; Tan, C.W. A comprehensive review of maximum power point tracking algorithms for photovoltaics systems. *Renew. Sustain. Energy Rev.* **2014**, *37*, 585–598. [CrossRef]
5. Esram, T.; Chapman, P.L. Comparison of photovoltaic array maximum power point tracking techniques. *IEEE Trans. Energy Convers.* **2007**, *22*, 439–449. [CrossRef]
6. Hohm, D.P.; Ropp, M.E. Comparative study of maximum power point tracking algorithm algorithms. *Prog. Photovolt. Res. Appl.* **2003**, *11*, 47–62. [CrossRef]
7. Femia, N.; Petrone, G.; Spagnuolo, G.; Vitelli, M. Optimization of perturb and observe maximum power point tracking method. *IEEE Trans. Power Electron.* **2005**, *20*, 963–973. [CrossRef]
8. Femia, N.; Grandozio, D.; Petrone, G.; Spagnuolo, G.; Vitelli, M. Predictive & adaptive MPPT perturb and observe method. *IEEE Trans. Aerosp. Electron. Syst.* **2007**, *43*, 2629–2637.
9. Femia, N.; Petrone, G.; Spagnuolo, G.; Vitelli, M. A technique for improving P&O MPPT performances of double-stage grid-connected photovoltaic systems. *IEEE Trans. Ind. Electron.* **2009**, *56*, 4473–4482.
10. Femia, N.; Petrone, G.; Spagnuolo, G.; Vitelli, M. *Power Electronics and Control Techniques for Maximum Energy Harvesting in Photovoltaic Systems*; CRC Press: Boca Raton, FL, USA, 2012.
11. Wyatt, J.; Chua, L. Nonlinear resistive maximum power theorem with solar cell application. *IEEE Trans. Circuits Syst.* **1983**, *30*, 824–828. [CrossRef]
12. Kivimäki, J.; Kolesnik, S.; Sitbon, M.; Suntio, T.; Kuperman, A. Design guidelines for multi-loop perturbative maximum power point tracking algorithms. *IEEE Trans. Power Electron.* **2018**, *33*, 1284–1293. [CrossRef]
13. Kivimäki, J.; Sitbon, M.; Kolesnik, S.; Suntio, T.; Kuperman, A. Revisited perturbation frequency guideline for direct fixed-step maximum power point tracking algorithms. *IEEE Trans. Ind. Electron.* **2017**, *64*, 7532–7541. [CrossRef]
14. Esram, T.; Kimball, J.; Krein, P.; Chapman, P.; Midya, P. Dynamic maximum power point tracking of photovoltaic arrays using ripple correlation control. *IEEE Trans. Power Electron.* **2006**, *21*, 1282–1291. [CrossRef]
15. Hussein, K.H.; Muta, I.; Hoshino, T.; Osakada, M. Maximum photovoltaic power tracking: An algorithm for rapidly changing atmospheric conditions. *IEE Proc.-Gener. Transm. Distrib.* **1995**, *142*, 59–64. [CrossRef]
16. Elgendy, M.A.; Zahawi, B.; Atkinson, D.J. Assessment of the incremental conductance maximum power point tracking algorithm. *IEEE Trans. Sustain. Energy* **2013**, *4*, 108–117. [CrossRef]
17. Kjær, S.B. Evaluation of the "hill climbing" and the "incremental conductance" maximum power point trackers for photovoltaic power systems. *IEEE Trans. Energy Convers.* **2012**, *27*, 922–929. [CrossRef]
18. Shmilovitz, D. On the control of photovoltaic maximum power point tracker via output parameters. *IEE Proc.-Electr. Power Appl.* **2005**, *152*, 239–248. [CrossRef]
19. Jiang, Y.; Qahouq, J.A.A.; Haskew, T.A. Adaptive step size with adaptive-perturbation-frequency digital MPPT controller for a single-sensor photovoltaic solar system. *IEEE Trans. Power Electron.* **2013**, *28*, 3195–3205. [CrossRef]
20. Elgendy, M.A.; Atkinson, D.J.; Zahawi, B. Experimental investigation of incremental conductance maximum power point tracking algorithm at high perturbation rate. *IET Renew. Power Gener.* **2016**, *10*, 133–139. [CrossRef]
21. Elgendy, M.A.; Zahawi, B.; Atkinson, D.J. Operating characteristics of P&O algorithm at high perturbation frequencies for standalone PV systems. *IEEE Trans. Energy Convers.* **2015**, *30*, 189–198.
22. Abdelrahman, A.K.; Massoud, A.M.; Ahmed, S.; Enjeti, P.N. High-performance adaptive perturb and observe MPPT technique for photovoltaic-based microgrids. *IEEE Trans. Power Electron.* **2011**, *26*, 1010–1021.
23. Kumar, N.; Hussain, I.; Singh, B.; Panirahi, B.K. Self-adaptive incremental conductance algorithm for swifth and ripple-free maximum power harvesting from PV array. *IEEE Trans. Ind. Informat.* **2018**, *14*, 2031–2041. [CrossRef]
24. Amer, E.; Kuperman, A.; Suntio, T. Direct fixed-step maximum power point tracking algorithms with adaptive perturbation frequency. *Energies* **2019**, *12*, 399. [CrossRef]
25. Schmidt, H.; Burger, B.; Bussemas, U.; Elies, S. How fast does an MPP tracker really need to be? In Proceedings of the European PV Solar Energy Conference, Hamburg, Germany, 21–25 September 2009; pp. 3273–3276.
26. Lappalainen, K.; Valkealahti, S. Recognition and modelling of irradiance transitions caused by moving clouds. *Sol. Energy* **2015**, *112*, 55–67. [CrossRef]

27. Lappalainen, K.; Valkealahti, S. Photovoltaic mismatch losses caused by moving clouds. *Sol. Energy* **2017**, *158*, 455–461. [CrossRef]
28. Lappalainen, K.; Valkealahti, S. Effect of PV array layout, electrical configuration and geographical orientation on mismatch losses. *Sol. Energy* **2017**, *144*, 548–555. [CrossRef]
29. Kivimäki, J.; Suntio, T.; Kuperman, A. Factors affecting validity of PVG-power settling time estimation in designing MPP-tracking perturbation frequency. In Proceedings of the IEEE Industrial Electronics Society Annual Conference, Beijing, China, 29 October–1 November 2017; pp. 2485–2491.
30. Lyi, S.; Dougal, R.A. Dynamic multiphysics model for solar array. *IEEE Trans. Energy Convers.* **2002**, *17*, 285–294.
31. Xiao, W.; Ozog, N.; Dunford, W.G. Topology study of photovoltaic interface for maximum power point tracking. *IEEE Trans. Ind. Electron.* **2007**, *54*, 1696–1704. [CrossRef]
32. Graditi, G.; Adinolfi, G.; Femia, N.; Vitelli, M. Comparative analysis of synchronous rectification boost and diode rectification boost converter for DMPPT applications. In Proceedings of the IEEE International Symposium on Industrial Electronics, Gdansk, Poland, 27–30 June 2011; pp. 1000–1005.
33. Suntio, T.; Messo, T.; Aapro, A.; Kivimäki, J.; Kuperman, A. Review of PV generator as an input source for power electronic converters. *Energies* **2017**, *10*, 1076. [CrossRef]
34. Viinamäki, J.; Jokipii, J.; Messo, T.; Suntio, T.; Sitbon, M.; Kuperman, A. Comprehensive dynamic analysis of photovoltaic generator interfacing DC-DC boost power stage. *IET Renew. Power Gener.* **2015**, *9*, 306–314. [CrossRef]
35. Viinamäki, J.; Suntio, T.; Kuperman, A. Grid-forming-mode operation of boost-power-stage converter in PV-generator-interfacing applications. *Energies* **2017**, *10*, 1033. [CrossRef]
36. Suntio, T.; Messo, T.; Puukko, J. *Power Electronic Converters—Dynamics and Control in Conventional and Renewable Energy Applications*; Wiley VCH: Weinheim, Germany, 2017.
37. Ogata, K. *Modern Control Engineering*; Prentice Hall: Upper Saddle River, NJ, USA, 1997.
38. Middlebrook, R.D. Design techniques for preventing input-filter oscillations in switched-mode regulators. In Proceedings of the National Solid-State Power Conversion Conference (Powercon 5), San Francisco, CA, USA, 4–6 May 1978; pp. A3.1–A3.16.
39. Suntio, T.; Leppäaho, J.; Huusari, J.; Nousiainen, L. Issues on solar-generator interfacing with current-fed MPP-tracking converters. *IEEE Trans. Power Electron.* **2010**, *25*, 2409–2419. [CrossRef]